This is the peer-reviewed, final accepted version for American Mineralogist, published by the Mineralogical Society of America.
The published version is subject to change. Cite as Authors (Year) Title. American Mineralogist, in press.
DOI: https://doi.org/10.2138/am-2022-8024. http://www.minsocam.org/

Revision 1: Ground-truthing the pyrite trace element proxy in modern euxinic settings

Gregory, Daniel D.[1], Lyons, Timothy W.[2], Large, Ross R.[3], and Stepanov, Aleksandr S.[4]

[1]Department of Earth Sciences, Earth Sciences Centre, 22 Russell Street, Toronto, ON M5S 3B1, Canada

[2]Department of Earth Sciences, University of California, Riverside, CA 92521, USA

[3]CODES Centre for Ore Deposit and Earth Sciences, Private Bag 126, University of Tasmania, Hobart, TAS 7001, Australia

[4]Collaborative Innovation Center for Exploration of Strategic Mineral Resources, Faculty of Earth Resources, China University of Geosciences, Wuhan 430074, China.

Abstract

Pyrite trace element (TE) chemistry is now widely employed in studies of past ocean chemistry. Thus far the main proof of concept has been correlation between large datasets of pyrite and bulk analyses emphasizing redox sensitive TE data from ancient samples spanning geologic time. In contrast, pyrite TE data from modern settings are very limited. The sparse available data are averages from samples from the Cariaco Basin without stratigraphic resolution and from estuarine sediments. To fill this gap, we present TE data (Co, Ni, Cu, Zn, Mo, Ag, Pb, Bi) from the two largest euxinic basins on Earth today, locations where the majority of the pyrite formed within the water column, the Black Sea and Cariaco Basin. These locations have different water column TE contents due to their relative degrees of restriction from the open ocean, thus providing an ideal test of the relationship between pyrite precipitated under euxinic conditions from basins with different degrees of basin restriction and dissolved TE concentration.

At each site we observed that down-core trends for pyrite increase before reaching relatively steady values for most TE. This observation suggests that instead of all the TE being sourced directly from the water column some are incorporated from the sediments, presumably desorbing from detrital materials. However, since much of the adsorbed TE are adsorbed from the overlying water, the pyrite chemistry still seems to reflect the water chemistry at or near the surface, indeed, for Mo, there is less variation in pyrite than in bulk sediment. Additionally, we found that pyrite formed during diagenesis due to sulfide diffusion into iron-rich muds revealed low TE contents, except for siderophile elements likely to have been adsorbed onto Fe (hydr)oxides, highlighting the risk of potential false negatives from pyrite formed under these conditions. This relationship highlights the need for detailed understanding of the full context, including use of complementary geochemical data such as sulfur isotope trends, in efforts to use pyrite TE to interpret conditions in the global ocean.

Introduction

Pyrite TE contents are used in a variety of ways in the Earth sciences, ranging from understanding different mechanisms of ore deposit formation (Large, et al. 2007, Revan, et al. 2014, Genna and Gaboury 2015, Cook, et al. 2016, Gadd, et al. 2016, Mukherjee and Large 2017, Gadd, et al. 2019) to tracing deleterious construction materials to their source (Dornan, et al. 2020) to tracing past ocean

chemistry (Large, et al. 2014, Gregory, et al. 2017, Mukherjee, et al. 2019). However, a rigorous understanding of when and how TE are incorporated into sedimentary pyrite remains illusive.

Several studies have addressed TE incorporation into sedimentary pyrite. In the earliest of those studies, chemical analyses of sequential leaches of bulk sediments were used to isolate the pyrite fraction for subsequent elemental analysis (Huerta-Diaz and Morse 1990, Huerta-Diaz and Morse 1992) and how the TE concentration changed with distance below the sediment-seawater interface. While useful in understanding which phase held different TE, a lack of specificity of the reagents used, a problem commonly encountered with sequential extractions (Martin, et al. 1987), frustrated these efforts. Next, pyrite was isolated for analysis by rock crushing, treatment with different chemicals, and hand picking of pyrite grains (Tribovillard, et al. 2008, Berner, et al. 2013, Pisarzowska, et al. 2014). While this approach was effective, the method was time consuming. Further, different textures of pyrite, which are often very small, were difficult to extract. For example, the small framboidal pyrite, like those analyzed in this study, were the most difficult if not impossible to isolate (Berner, et al., 2013). More recently the adoption of laser ablation inductively coupled plasma mass spectrometry (LA-ICPMS) analyses has allowed in situ analysis of fine pyrite grains and thus focus on specific pyrite types. This methodology has been used to explore long-term trends in ocean chemistry (Large, et al. 2014, Gregory, et al. 2017, Large, et al. 2019, Stepanov, et al. 2020). This technique has the potential to overcome some common difficulties encountered with traditional ocean chemistry proxies. First, sedimentary pyrite is ubiquitous in the geological record so obtaining complete datasets is relatively straight forward for much of Earth history. Second, sedimentary pyrite TE content can be preserved up to greenschist facies metamorphism (Large, et al. 2007, Gregory, et al. 2016) whereas this can frustrate whole rock studies due to potential for metal remobilization (Ardakani et al., 2016). Finally, because sedimentary pyrite is precipitated directly out of the water column or pore waters it is not as susceptible to dilution from detrital components as traditional whole rock proxies. That said this technique is not without its difficulties. Pyrite formed in euxinic conditions tend to be small (Wilkin et al., 1996; Rickard et al., 2019) which makes them difficult to analyze. However, even though most framboids are small (geometric mean 4.7 µm; Rickard et al., 2019) the range of syngenetic (water column formed) pyrite is 2.9-10.9 µm. It is the larger end of this range, or clusters of smaller framboids, that were the focus of this study. Rickard et al., (2019) also argued that pyrite framboids do not get additional pyrite added to them (at least not such that there would not be a textural difference) so we are confident that the chemistry of these framboids is representative of the pyrite framboids in the sample.

Thus far the LA-ICPMS approach to pyrite analyses has been applied almost exclusively to black shales from ancient sediments. These have shown agreement with several other widely used paleoceanographic proxies, such as Ni in banded iron formations (Konhauser, et al. 2017) and molybdenum in euxinic black shales spanning billions of years (Scott, et al. 2008). This agreement has also been demonstrated at the scale of an individual stratigraphic section (Wuhe, Doushantuo Formation, China) where pyrite TE analysis has been shown to match traditional whole rock proxies such as Mo, U, and Re concentration (Sahoo, et al. 2016, Gregory, et al. 2017). Recent Mo isotope data from the Wuhe section specifically suggest changes in connectivity to the global ocean over the duration of deposition and by inference that variations in pyrite elemental data capture local rather than global effects (Ostrander, et al. 2019). This example points to the possibility that both the pyrite proxy and traditional whole rock data are vulnerable to local controls. One goal of this study is to examine the

degree to which local controls affect pyrite trace element chemistry by comparing a more restricted basin (Black Sea) with a less restricted basin (Cariaco Basin).

To date, only limited analyses have been conducted on pyrite forming in modern ocean waters where the TE content of the water from which the pyrite formed can be known or at least approximated. Some analyses from the Cariaco Basin were undertaken as part of the original proof of concept for the pyrite proxy (Chappaz, et al. 2014, Large, et al. 2014, Gregory, et al. 2015); however, these lacked stratigraphic context. Some stratigraphic analyses were performed to compare between the metal-rich Derwent and metal-poor Huon Estuaries (Gregory, et al. 2013, Gregory, et al. 2014). However, these efforts addressed extremes linked to anthropogenic metal contamination, and while they showed that the pyrite technique was sensitive to changes in metal abundance, a lack of pore water analyses meant that the more subtle relationship between availability of TE and degree of enrichment in pyrite could not be determined.

In this contribution we have obtained samples from the two largest euxinic basins in the modern world, the Black Sea and the Cariaco Basin, which have been euxinic for the past ~8.0 and 14.5 ka BP, respectively (Lyons et al., 2003; Arthur and Dean 1998). Euxinic basins were chosen for this study because the pyrite is likely to have formed largely in the water column (Wilkin, et al. 1996), giving it the best chance of accurately reflecting the TE chemistry of that water. Furthermore, these sites are ideal because the Cariaco Basin is recharged from the Caribbean Sea, while the Black Sea is highly restricted, resulting in pronounced differences in the TE contents of the waters in the two basins (Jacobs, et al. 1987, Haraldsson and Westerlund 1988, Emerson and Huested 1991, Colodner, et al. 1995), with generally significantly lower TE concentrations in the Black Sea (Algeo and Lyons, 2006; Scott and Lyons, 2012), though surface waters have similar Mo concentrations once corrected for salt content (Algeo and Lyons, 2006). These differences allow assessment of the sensitivity of TE content of pyrite to changes in local inventories relative to global availability. Additionally, because the samples have strong stratigraphic control, any temporal differences that may reflect changing local conditions can be identified, including fundamental shifts in depositional redox and associated pyrite overprints.

Pyrite Formation

Pyrite forms when sulfidic conditions are present in the water column or in sediments. Several pathways have been proposed for pyrite formation, and each of those pathways depends on different precursor phases that the resultant pyrite might inherit TE from. Thus, to fully understand the TE concentration of the resultant pyrite, a discussion of how pyrite forms in sediments is needed. A brief summary of how this occurs is presented here, but for a detailed discussion see Rickard (2012) and references therein. Pyrite formation can be summarized via three main reaction pathways:

(1) $FeS + H_2S \rightarrow FeS_{2(pyrite)} + H_2$ (Rickard 1975, Rickard 2012)
(2) $FeS + S^{2-}_n \rightarrow FeS_{2(pyrite)} + S^{2-}_{(n-1)}$ (Rickard 1975, Rickard 2012)
(3) Complex, potentially variable, reactions involving sulfidation of Fe (hydr)oxides (Peiffer, et al. 2015)

Reaction 1 involves the reaction of H_2S with FeS, a solid precursor such as mackinawite or a dissolved FeS species. However, it has been argued, although often cited as a precursor, that mackinawite is not likely to form in modern sedimentary environments (Rickard and Morse 2005). Further, slight oxidation of FeS is needed for the reaction to proceed (Benning, et al. 2000, Swanner, et al. 2019). Reaction 1 is

more likely to occur at moderate to low pH (Rickard and Morse 2005), because these pH conditions stabilize the H_2S and HS^-. At higher pH, reaction 2 predominates as the H_2S concentration, relative to HS^- and S^{2-}, approaches 0, although with slower reaction rates (Rickard and Morse 2005). Reaction 3, while important in some settings may be less important for most of the pyrite analyzed here, which is thought to form in the water column, predominantly at the interface between sulfidic waters and the overlying non-sulfidic waters (Lyons 1997). That said, this pathway is likely much more important in the lower most Cariaco Basin samples where sulfidic water has diffused into the underlying sediments that were deposited in a non-sulfidic environment and were likely rich in Fe oxides (Lyons, et al. 2003).

In addition to the requisite reactions, two more processes are needed for pyrite formation. These are nucleation of the pyrite grain and growth by addition of more Fe and S atoms to the initial nucleated mass (Rickard, 2012). The formation of the initial pyrite requires a high degrees of supersaturation; additional later pyrite can form at lower degrees of supersaturation in the presence of seed crystals (Harmandas, et al. 1998, Rickard 2012). Other factors may also affect nucleation rates. Biology has the ability to greatly enhance pyrite formation rates; 10^4 to 10^5 times faster reaction rates have been found in S-isotope studies (Canfield, et al. 1998). Even passive presence of biological materials may be important for pyrite formation. Mackinawite has been found to nucleate on live and dead remains of sulfate reducing bacteria, and it is plausible that it may play a similar function for pyrite (Picard, et al. 2017). Trace elements might also affect pyrite formation rates. For example, Morin, et al. (2017) found that the presence of Ni greatly enhanced the rate of pyrite formation in their experiments.

Pyrite trace element incorporation

Pyrite has long been recognized as a sink for many TE, especially the chalcophile and siderophile elements. However, the manner in which these elements are incorporated (i.e., inclusions vs. structurally bound) into the pyrite is less well understood. Based on water exchange reaction rates, it has been argued that Ni and Co, with relatively slow water exchange kinetics are more likely to be incorporated into the pyrite structure (Morse and Arakaki 1993), while elements with faster water exchange kinetics (e.g., Zn) are more likely to form nano-inclusions (Morse and Arakaki, 1993). Inspection of time resolved laser ablation output graphs has broadly supported this interpretation (Gregory, et al. 2014, Gregory, et al. 2015). However, it should be noted that neither of these techniques have the resolving power to remove uncertainties, and further analyses are required to distinguish between structurally held TE and those hosted in evenly distributed nano-inclusions.

How these TE are held may affect the ability of the TE to accurately reflect the chemistry of the fluids in which the pyrite formed because the specific mineral phase involved may affect the partition coefficients and thus our interpretation of the past ocean chemistry. This relationship has been particularly well studied for As, and we use it here as an example of how one TE may affect how others are incorporated. Arsenic can be incorporated into pyrite via three main mechanisms: As (-I) substitution for S(-II) (Reich and Becker 2006), As (III) substitution for Fe (II) (Deditius, et al. 2008, Qian, et al. 2013), and as nano-inclusions of amorphous As-Fe-S (Deditius, et al. 2008). Each of these mechanisms may affect how other TE are incorporated into the pyrite and thus the degree of enrichment in pyrite compared to the amount of enrichment of the surrounding fluids. For example, As (III) substitution for Fe (II) results in a charge imbalance, which leads to a vacancy in the pyrite structure, thus creating space necessary for the incorporation of large anions (Cook and Chryssoulis 1990, FLEET 1997). Conversely, if

the As (-I) replaces S (-II), the result is an increase of elements with ionic radii similar to Fe(II) (i.e., Co(II), Ni(II), Cu(II)) (Michel, et al. 1994, Deditius, et al. 2008) in the pyrite.

Molybdenum is of particular importance when discussing both the TE content of pyrite and its use in determining past ocean chemistry because it is redox sensitive and has a long ocean residence time. Further, significant removal is tightly tied to euxinic areas in the oceans (Tribovillard, et al. 2006). Because of this reservoir relationship, in sediments deposited under local euxinic conditions, elevated Mo contents—much as are observe in the Cariaco Basin today—have been used to infer periods of widespread oxygenation (Lyons, et al. 2003, Tribovillard, et al. 2006, Scott, et al. 2008, Asael, et al. 2017). Furthermore, because much of the Mo in the ocean derives from oxidative weathering of sulfide minerals on land, the earliest increases in Mo concentrations in euxinic shales are taken as signs of initial atmospheric oxygenation (Scott, et al. 2008) and transient events leading up to that 'Great Oxidation Event' (Anbar, et al. 2007, Gregory, et al. 2015). Further, relatively low Mo concentrations in black shales at times of widespread ocean oxygenation are assumed to reflect local basin restriction (Algeo and Lyons 2006).

How Mo is contained within pyrite is still in question it has been suggested that rather than being incorporated by substitution into pyrite Mo forms Fe-Mo-S colloids which are then accumulated into sediments (Helz and Vorlicek, 2019 and Vorlicek et al., 2018). However, Chappaz et al. (2014) have shown that while a significant amount of Mo is incorporated in matrix material pyrite is still relatively enriched in Mo. While we acknowledge that this is still an active area of research the LA-ICPMS techniques does not give us the resolution to determine how Mo is incorporated into pyrite and we will discuss Mo in pyrite as the amount of Mo that was present in the pyrite ablation volume.

Methods

Samples

The samples from the Cariaco Basin were taken from approximately 900 m depth from site 1002 during Leg 165 of the International Ocean Discovery Program (IODP) cruise in 1996. Following pore water extraction, the samples were frozen continuously until dried, which will have minimized additional reactions between the pyrite in the sample and matrix material. The stratigraphic section from site 1002 has 3 main components. The top unit is approximately 6.5 m thick. It is finely laminated (1 mm to sub-mm thick) and dark olive gray with no evidence of bioturbation (Lyons et al., 2003). This unit has evidence of minor (at most a few % of section) thin (1-2 cm) turbidities. The unit can be subdivided into two subunits based on a transition from nannofossils and foraminifera to diatoms and abundant calcareous microfossils at approximately 4.2 m which corresponds to the end of the Younger Dryas cold period (Lyons et al., 2003). These sub-units were both deposited during the recent 14.5 kyr episode of persistent euxinia in the Cariaco Basin (Lyons, et al., 2003). Below the interval of sediments deposited under euxinic conditions is a massive bioturbated light gray clay interval which is in turn underlain by a massive, bioturbated reddish-brown clay layer. It has been interpreted that both these layers were deposited under oxic conditions but the light gray clay was reduced by diffusion of sulfidic water from the overlying sediments that were deposited under euxinic conditions (Lyons, et al. 2003).

The Black Sea samples were collected during the UNESCO International Oceanography Commission (IOC) training through research cruise in 2001 (Logachev et al., 2002). Samples were taken from two cores. BS-330B (44°18.789', 35°04.379) sampled the upper layer of the unit I; in this core the sediment seawater

interface was recovered in tack. BS-315G (43°20.324', 33°26.752') over penetrated and the upper most sediments were lost but samples from the lower part of unit I and II were obtained (Kenyon et al., 2001). These samples were frozen after collection. The euxinic interval in the Black Sea is separated into two units, I and II. Unit I consists of finely laminated light (mm scale), calcium carbonate rich layer and dark-gray to black layers (Lyons and Berner, 1992). Unit II is homogeneous, dark-gray, organic rich argued to be due to re-sedimentation of the Black Sea basin margin sediments (Lyons et al., 1992). In core BS-315G the contact between unit 1 and unit 2 occurs at 25 cm. Both units I and II are regionally extensive and were deposited under euxinic conditions (Lyons 1991).

Both the Cariaco Basin and Black Sea samples were subsampled, and the material was mounted in EpoThin epoxy resin under vacuum and subsequently polished using 1 µm diamond paste.

SEM

Images were collected of pyrite framboids from the Cariaco basin mounted in epoxy using scanning electron microscopy (SEM) with back-scattered electron imaging (Fig. 1). Prior to analysis, samples were coated with carbon to avoid charge build up. Analyses were carried out in the Central Facility for Advanced Microscopy and Microanalysis at the University of California, Riverside, using a NovaNanoSEM 450.

LA-ICPMS

The pyrite framboids were analyzed for TE content at the University of Tasmania using a 193 nm ArF excimer ATL Atlex ILR laser coupled with an Agilent 7700 ICP-MS. Twenty 2.5 cm laser mounts (including three standard blocks) were placed in the constant-geometry Laurin Technic ablation chamber where pyrite framboids or clusters of framboids were ablated with 13 µm laser spots with a pulse rate of 5 Hz in a pure He atmosphere (flow rate 0.85 l/min). Due to the small size of the pyrite framboids, a smaller spot size was used compared to many previous studies. Thus, the detection limits were higher, and we did not measure low abundance elements such as Au. The ablated material was mixed with Ar (0.85 l/min) immediately past the ablation point to improve the efficiency of aerosol transport. The masses between 80-240 amu were optimized in the ICP-MS as these were the mass ranges of greatest interest.

Due to the small size of the pyrite framboids, invariably some matrix (sedimentary material) was ablated with the pyrite. Any analyses with more than 30% matrix (as determined by idealized oxide composition of lithophile elements) were deleted. Remaining analyses were corrected for matrix composition using an algorithm-based linear regression similar to that described in Stepanov et al. (2020) and Gregory et al. (2017). In brief, this method segments the signal relative to time of ablation and uses those segments to calculate an initial composition of the matrix and pyrite followed by recalculation of the compositions to 100% sum of chalcophile elements and oxides for lithophile elements. After this, the new compositions are plotted against S, and a linear regression equation was used to calculate the matrix-free pyrite composition. Iron was used as the internal standard for data reduction and stoichiometric Fe concentration was assumed. Three different standards, with two analyses of each were analyzed every 15 samples and at the beginning and end of each analytical session. Three standards were used to ensure that all elements of interest had a standard with an appropriate concentration and similar ablation behavior. For S, stoichiometric Peruvian pyrite was used (^{34}S; (Gilbert, et al. 2014). GSD-1G (Guillong, et al. 2005) was used for the lithophile elements (^{24}Mg, ^{27}Al, ^{29}Si, ^{43}Ca, ^{49}Ti, ^{51}V, ^{55}Mn, ^{59}Co, ^{60}Ni, ^{90}Zr, ^{157}Gd, ^{178}Hf, ^{181}Ta, ^{182}W, ^{232}Th, ^{238}U), and STGL2b2 (Danyushevsky, et al. 2011) was used for the

chalcophile and siderophile elements (^{65}Cu, ^{66}Zn, ^{75}As, ^{77}Se, ^{95}Mo, ^{107}Ag, ^{111}Cd, ^{118}Sn, ^{121}Sb, ^{125}Te, ^{195}Pt, ^{197}Au, ^{202}Hg, ^{205}Tl, ^{206}Pb, ^{207}Pb, ^{208}Pb, ^{209}Bi).

Results

The pyrite analyzed was all framboidal (Fig. 1) except for samples from the sulfide overprint zone in the Cariaco Basin where some pyrite formed later euhedral overgrowths on the earlier framboidal pyrite. In the latter case the euhedral overgrowths and the framboidal centers were analyzed together as the pyrite grain was too small for the laser beam to be used to selectively analyze the different parts of the framboid. Most framboids were ~10 µm in diameter, although exact diameter of the sphere was difficult to estimate due to the 2-D nature of polished blocks. Of the 150 total Cariaco Basin analyses, 73 had to be discounted due to over 30% matrix content. Similarly, of the total 138 Black Sea pyrite analyses, 88 had to be discounted due to over 30% matrix content. Future studies should expect a similar number of analyses to have to be discounted due to elevated matrix inclusions within their analyses and should plan their sampling strategy accordingly.

The TE content of pyrite is plotted against depth of sample in Fig. 2 for the Cariaco Basin and Fig. 3 and 4 for the Black Sea, and these data are summarized as medians and median absolute deviation in tables 1, 2, and 3. Median error estimates (1 σ) for the analyses are in table 4. Pyrite trace element content is rarely, if ever, normally data distributed so summarizing the data as a mean and standard deviation is inappropriate (Gregory, et al. 2019, 2020). While in some cases pyrite trace element abundance is lognormal so geometric means and multiplicative standard deviations can be used our data set is too small to be confident that the distribution is lognormal (Gregory, et al. 2015) so instead we summarize the data using the median and median absolute deviation. If analyses were below the detection limits, half of the detection limit was used instead when calculating median values. It should be noted that, while pyrite was present, too few framboids of sufficient size were available to allow for analysis of pyrite framboids from the sediments deposited during the Younger Dryas period (Cariaco Basin; Lyons et al., 2003). In the discussion of the data presented here we use medians and median absolute deviation (MAD) to compare data between different stratigraphic intervals. If a specific interval is less than the median for the entire data set minus the MAD for the entire dataset it is taken to be a significant depletion in that element. Thus, hence forth “significant depletion” will refer to analyses that are below the median minus MAD for the entire dataset. Similarly, if the median of analyses from a specific depth is greater than the median for the entire dataset plus the MAD for the entire dataset it is taken to be a significant enrichment.

Cariaco Basin

In the Cariaco Basin, the pyrite TE concentrations tend to be lower in the top 1 to 3 samples (0-5 cm, 25-30 cm, and 40-45 cm, respectively; Fig. 5). The TE also decrease at the transition from oxic to euxinic deposition marked by a sulfide overprint on the uppermost oxic layers. Cobalt is initially significantly depleted in concentration and slowly rises in the first three samples (to a depth of 42.5 cm; Fig. 2). Further, only one of the other samples deposited under euxinic conditions had significantly depleted Co content, ranging from 15.4 to 110 ppm, with the majority between 15 and 39 ppm. The one significantly depleted sample had a median of 5.49 ppm, but this sample had only two viable analyses, and these low concentrations may be outliers. In the zone of sulfide diffusion, the Co content is similar to the euxinic interval (medians of 22.0 to 76.8 ppm) except for the lowest sample (median of 8.1 ppm Co). Nickel is relatively low in the first three samples (with two significantly depleted; 93.0 and 40.9 ppm), while the

rest of the euxinic interval is not significantly depleted, ranging from 164 to 667 ppm Ni. Again, like Co, Ni in all but the deepest sample in the sulfide diffusion zone is not significantly depleted, ranging from 229 to 303 ppm Ni, while the deepest sample is markedly low with 21.1 ppm Ni. The Pb content follows a similar trend to the Ni content, with two of the three shallowest samples having significantly depleted Pb values (15.3 and 22.7 ppm), and the lowest most sample is also significantly depleted in Pb (11.5 ppm). The rest of the analyses range from medians of 32.7 to 128 ppm Pb.

For Cu, the first two samples have medians (27.6 and 93.9 ppm) that are significantly depleted. The other pyrite deposited under euxinic conditions, except for one that is anomalously high, range from 183 to 894 ppm. Different from Co and Ni, pyrite in the sulfide diffusion zone shows a rapid decrease in TE content with increasing distance from the interval deposited under euxinic conditions (from 193 ppm to 14.1 ppm Cu). A similar trend is observed with Mo, where the top most sample has a median Mo content (168 ppm) that is significantly depleted and a sharp decrease in the sulfide diffusion zone (steady decrease with median of 75.3 ppm near the interface with the sediments deposited under euxinic conditions to 4.02 ppm in the deepest sample). The rest of the euxinic interval had Mo content that were not significantly depleted. Except for a high and low outlier, the median of the analyses in the interval deposited under euxinic conditions ranged from 698 ppm to 1490 ppm Mo. The low outlier was from the -610 cm interval and had only one analysis, so it may not be representative of the sample. There is one sample in the euxinic interval that has markedly high Cu and Mo content (1850 ppm and 2310 ppm, respectively); however, this is the same sample that had the low Co and may be due to a low number of analyses in that sample.

Silver is relatively enriched and depleted in the same intervals as Mo, with a significantly depleted concentration in the top samples (with all but one analysis below detection) and in the sulfide diffusion interval (decreasing from 1.49 ppm near the interface with the euxinic interval to 0.24 ppm in the deepest sample). As for Mo, there is a relative enrichment at -362.5 cm (median of 36.8 ppm Ag) and a depletion at -610 cm (median of 0.71 ppm Ag). Again, these intervals had few viable analyses and may not reflect the true median TE composition of the framboids found there. The median Ag content of the other samples found within the euxinic interval all have values that are not significantly depleted, ranging from 2.50 to 22.3 ppm. Bismuth shows enrichments at depths similar to those for the enrichments of Cu, Mo, and Ag. Bismuth has medians that are significantly depleted in the first two samples (with all but one analysis below detection limits) and the last four samples from the sulfide diffusion zone, decreasing from 0.73 ppm at -670 cm to 0.23 ppm at -725 cm.

Zinc shows behavior in the sulfide diffusion zone similar to the observations for Cu, Mo, Ag, and Bi, with three of the five samples significantly depleted. However, it differs in that all but one of the samples deposited under euxinic conditions are not significantly depleted for the entire Cariaco dataset (ranging from medians of 434 to 1020 ppm Zn). The one data point in the euxinic interval with 205 ppm is from a single analysis and may not be representative of all the pyrite in that sample.

Black Sea

Core 315

The median values in core 315 from the Black Sea all have only the top two samples significantly depleted for Co, Ni, and Cu (37.5 and 51.3 ppm; 212 and 129 ppm; and 566 and 467 ppm for Co, Ni, and Cu respectively; Fig. 3). The rest of the samples ranged from 84.6 to 1340 ppm, 473 to 1450 ppm, and

647 to 1740 ppm for Co, Ni, and Cu, respectively. Zinc and Bi were similar, however, in that only one of the top two samples was significantly depleted (77.8 and 2.42 ppm for Zn and Bi from this top sample, respectively). Neither Ag nor Pb have medians of analyses from a specific interval significantly depleted. Median values for Ag and Pb range from 2.53 to 6.61 ppm for Ag and 61.3 and 194 ppm for Pb. Molybdenum is similar to Co, Ni, and Cu. It has medians in the top two samples significantly depleted (683 and 428 ppm).

Core 330

Core 330 shows fewer clear trends than 315 (Fig. 4). The only elements with median values from a specific stratigraphic level significantly depleted are the Co, Ni, Cu and Mo in the uppermost sample (18.3, 18.0, 58.6, and 54.1 ppm for Co, Ni, Cu, and Mo, respectively). The other intervals have medians that range from 42.3 to 964 ppm for Co, 127 to 595 ppm for Ni, 149 to 754 for ppm Cu, 110 to 434 ppm for Zn, 302 to 1332 ppm for Mo, 1.59 to 3.59 ppm for Ag, 44.1 to 208 ppm for Pb, and 2.15 to 3.56 ppm for Bi. Importantly, the median values for all the elements tend to be higher in 315 than in 330, with 427, 986, 1090, and 1220 ppm for Co, Ni, Cu, and Mo, respectively, in core 315, compared to 67.0, 195, 225, and 359 ppm, respectively, in core 330. Similarly, median values of the entire core for Ag and Bi are higher in core 315 compared to 330, but the variation is less extreme (medians for Ag and Bi in core 315 are 3.04 and 3.95 ppm, respectively, compared to 2.14 and 2.82 ppm in core 330). The only elements that show the opposite relationship are Zn and Pb, with slightly higher median values in core 330 (with medians for Zn and Pb in core 315 of 150 and 93.8 ppm, respectively, compared to 177 and 110 ppm in core 330).

Discussion

Cariaco basin

Relatively low abundances for many TE in the top three samples (to a depth of 45 cm; Fig. 5 and Table 1) were observed. Our low TE in pyrite (or TE pyritization) in the most shallow samples is similar to observations based on sequential leach analyses (Huerta-Diaz and Morse 1992) and discrete pyrite analyses in estuarine settings (Gregory, et al. 2014). In these cases, most TE in pyrite generally increase in abundance with increasing depth below the sediment-seawater interface prior to reaching roughly steady levels. Contrary to the idea that pyrite in euxinic settings inherit all of its TE content from the water in which it formed (Gregory et al., 2017), these data suggest that at least a portion of the TE are inherited from the sediments. That being said, as the TE in pyrite equilibrated relatively early, their abundances most likely reflect the contents of weakly bound elements likely adsorbed onto particles from the seawater (that is, the same water column) rather than being bound to detrital grains and transported into the basin. In this way, the pyrite data can capture water chemistry but through a somewhat complicated pathway.

Within the sulfide diffusion zone (Fig. 2), there is a significant difference in the texture of the pyrite, with coarser grained pyrite nucleating on earlier framboids (Fig. 1b) that precipitated at a higher degree of supersaturation—similar to those observed in Green Lake (Suits and Wilkin 1998). These textures are representative of secondary pyrite formation in the Cariaco Basin presumably due to additional Fe being available through Fe (hydr)oxides present in the oxic layers. In fact, sediments below this gray zone of sulfide diffusion are reddish brown from the presence of oxide phases (Lyons et al, 2003). This interpretation is supported by the TE trends observed moving down core. The contents of

most TE of interest decrease markedly below the euxinic interval and into the zone of sulfide diffusion, with a gradual decrease from the top to bottom of the sulfide diffusion zone (Fig. 2). Cobalt, Ni, and Pb are exceptions to this trend, in that they continue to be elevated in the sulfide diffusion zone (except for the deepest sample).

The reason for this exception is likely that at this stratigraphic position, the TE content is less a function of the TE in the ocean water and adsorbed onto euxinically deposited sediments and more a function of the TE contained within Fe (hydr)oxides. Because the TE abundance of Fe (hydr)oxides have not been measured in the Cariaco Basin, literature sources were consulted for the TE content of Fe crusts from the Atlantic Ocean, which show that Co, Ni, and Pb are the most enriched (means of 3608, 2581, and 1238 ppm respectively) (Koschinsky and Hein 2017)—the same elements that were enriched in pyrite in the sulfide diffusion zone in the Cariaco Basin. It should be noted, however, that the enrichments are more complicated than simply reflecting ambient abundance of TE, as the enrichments in the pyrite do not show the same ratios as the enrichments in the (Fe hydr)oxide crusts. Thus, it might be expected the TE patterns will agree much more closely if the pyrite formed via reaction 3. This relationship has an important implication for using pyrite TE chemistry as a proxy for past ocean chemistry—specifically, gray shales interbedded with black shales are potentially depleted in some TE and not others due to replacement of Fe (hydr)oxides by diffusion of sulfide from the organic rich intervals rather than reflecting changes in past ocean chemistry. Such secondary overprints might be expected anytime organic-rich and organic-lean sediments are juxtaposed, such as are observed in Mediterranean sapropels—often reflecting dramatic and abrupt changes in depositional conditions such as primary productivity and redox. That being said, because Fe (hydr)oxides can track broad, first-order ocean chemistry if their mineralogy is correctly identified and put in the correct context, pyrite formed via this mechanism may still allow some inferences to be made about ocean chemistry at the time of formation. Although, except in these ideal circumstances, grey and brown shales should be avoided when using the pyrite proxy method due to the potential for misinterpretation of the data.

Black sea

Core 330 is analogous to the top part of the Cariaco Basin interval, as it contains the uppermost sediments in Unit 1, the most recently deposited sediments in the Black Sea. However, it differs in that we were able to sample at a much higher stratigraphic resolution in the Black Sea. The data show a similar low relative TE abundance in the upper samples compared to the deeper intervals for Co, Ni, Cu, and Mo. It also appears that the core 330 samples have not yet equilibrated as the bottom samples of core 330 have medians for each of these elements that are much less than those of core 315. Core 315 samples a deeper part of unit 1 and unit 2. In core 315 Co, Ni, Cu, and Mo have median values of 427, 986, 1087, and 1220 ppm, respectively, compared to 67.0, 195, 225, and 359 ppm, respectively, in core 330. This trend is consistent with the Cariaco Basin samples where samples had not equilibrated until depths between 45 and 70 cm.

Core 315 over-penetrated and the top sediments were lost but a similar trend can still be observed. The upper most samples contain relatively low amounts of several TE in the top two samples, with Co, Ni, Cu, and Mo all being below the medians for the remainder of the core. These samples, like core 330 and the core from the Cariaco Basin also show that it takes time for the trace elements to accumulate in sedimentary pyrite after deposition, presumably due to desorption from organic matter

and other detritus during early diagenesis. This is similar to observations of TE enrichment in pyrite from organic rich, oxic depositional setting (Huon Estuary; Gregory et al., 2014).

Comparison of pyrite between the two basins

A comparison between the relatively open Cariaco Basin and the more restricted Black Sea is important to assess how the pyrite proxy may vary with different levels of basin restriction. For all elements of interest, except Co and Zn, the median TE content of pyrite from the equilibrated portion of the core varied by less than a factor of 3.1 between the two basins (Table 5). This is far less than the over an order of magnitude enrichments of TE in sedimentary pyrite that are currently being used to identify broad, first-order trends in ocean chemistry (Large et al., 2014; Gregory et al., 2017).

A common issue when interpreting TE data from bulk sample analyses is variations in concentration due to basin restriction. Here we focus the conversation of Mo, one of the more common elements used to interpret past ocean chemistry using bulk sample analysis (Tribovillard, et al. 2006 Scott et al., 2008) and also one that can be effective using pyrite data (Gregory et al., 2017). Averages of the Black Sea and Cariaco Basin bulk analyses of the euxinically deposited sediments are 45 and 85 ppm, respectively (Algeo and Lyons, 2003; Table 5)—that is, approximately half as much Mo accumulates in the bulk sediments of the more restricted Black Sea versus the less restricted Cariaco Basin. Conversely pyrite is more enriched in the Black Sea versus the Cariaco basin, although the discrepancy is less than that observed for the bulk sample analyses and in the opposite direction. Medians of pyrite from the Black Sea (from analyses with equilibrated pyrite concentrations) is 1.54 times that of the pyrite from the Cariaco Basin. Again, importantly, there is a relatively small difference in pyrite TE content between basins despite the very different degrees of restriction and bulk TE contents. This is likely because the Mo content of the surface waters are similar between the restricted Black Sea and less restricted Cariaco Basin when corrected for salinity (as summarized in Algeo and Lyons, 2006). The near surface environment, at the oxic/sulfidic water interface, is where most pyrite forms and where there is the steepest decrease in dissolved trace elements, suggesting that pyrite is an important TE sink. At the same time dissolved metals that show a systematic decrease across this interface also appear to be scavenged from the water column from detrital components (including organic matter) (Lewis and Landing 1992). Thus, the source of the Mo in the pyrite framboids is direct precipitation from the water column, and incorporation of Mo into pyrite early during sedimentation via desorption from detrital materials with a source of Mo from the upper, enriched, part of the water column that is similar to the open ocean concentrations. Therefore, even though the pathway involves both a direct precipitation pathway and a secondary enrichment pathway following desorption from detrital constituents, pyrite chemistry appears to track the chemistry of the overlying, oxic, water column.

Implications

Here it is shown that pyrite TE content, even in euxinic settings where most pyrite forms in the water column, is at least partially sourced from sediments. These TE adsorbed onto detrital material and still reflect the overlying water column but in a complex way compared to direct incorporation into pyrite in the water column. Importantly, at least for Mo, pyrite deposited under euxinic conditions TE content varies less between the Cariaco Basin and Black Sea than bulk sample analysis. This suggests that the pyrite proxy may be less sensitive to basin restriction than traditional bulk sediment analysis proxies, provided surface waters are similar. Because framboidal pyrite is unlikely to accumulate additional pyrite without the later pyrite having a significantly different texture (Rickard, 2019) this

study suggests that the TE chemistry of framboidal pyrite deposited under euxinic conditions is a valid proxy for past ocean chemistry.

It is also shown that large variation in TE content are present at interfaces between different depositional conditions, such as those marking changing depositional redox. This observation highlights the risk of mistaken interpretations in grey shales or samples from near lithologic boundaries where the pyrite TE content might better reflect the TE content of Fe (hydr)oxide minerals rather than the overlying sea water. We suggest grey and brown shales should not be used in pyrite proxy studies and only consistently black shales should be used for these purposes. That said, the relatively low variation in TE in pyrite between the two basins supports the use of pyrite TE chemistry to understand past ocean chemistry but also highlights the need for continued investigation of pyrite forming in modern settings and experimental work to better understand the relative enrichment factors of different elements into pyrite. With continued proxy validation and careful applications, we are confident that pyrite TE content can be an important tool to understand the chemistry of past oceans.

Acknowledgements

The authors would like to acknowledge support from the National Science Foundation Frontiers in Earth System Dynamics (NSF FESD) program and the National Aeronautics and Space Administration (NASA) Astrobiology Institute under cooperative agreement NNA15BB03A issued through the Science Mission Directorate. Also we acknowledge support from the Natural Sciences and Engineering Research Council (NSERC) Discovery Grant to Daniel Gregory (04834).

References

Algeo, T.J. and Lyons, T.W. (2006) Mo–total organic carbon covariation in modern anoxic marine environments: Implications for analysis of paleoredox and paleohydrographic conditions. Paleoceanography, 21.

Anbar, A.D., Duan, Y., Lyons, T.W., Arnold, G.L., Kendall, B., Creaser, R.A., Kaufman, A.J., Gordon, G.W., Scott, C., and Garvin, J. (2007) A whiff of oxygen before the great oxidation event? Science, 317, 1903-1906.

Ardakani, O.H., Chappaz, A., Sanei, H., and Mayer, B. (2016) Effect of thermal maturity on remobilization of molybdenum in black shales. Earth and Planetary Science Letters, 449, 311-20.

Arthur, M.A. and Dean, W.E. (1998). Organic-matter production and preservation and evolution of anoxia in the Holocene Black Sea. Paleoceanography, 13, 395-411.

Asael, D., Rouxel, O., Poulton, S., Lyons, T., and Bekker, A. (2017) Molybdenum record from black shales indicates oscillating atmospheric oxygen levels in the early Paleoproterozoic. American Journal of Science.

Benning, L.G., Wilkin, R.T., and Barnes, H. (2000) Reaction pathways in the Fe–S system below 100 C. Chemical Geology, 167, 25-51.

Berner, Z.A., Puchelt, H., NÖLtner, T., and Kramar, U.T.Z. (2013) Pyrite geochemistry in the Toarcian Posidonia Shale of south-west Germany: Evidence for contrasting trace-element patterns of diagenetic and syngenetic pyrites. Sedimentology, 60, 548-573.

Canfield, D.E., Thamdrup, B., and Fleischer, S. (1998) Isotope fractionation and sulfur metabolism by pure and enrichment cultures of elemental sulfur-disproportionating bacteria. Limnology and Oceanography, 43, 253-264.

Chappaz, A., Lyons, T.W., Gregory, D.D., Reinhard, C.T., Gill, B.C., Li, C., and Large, R.R. (2014) Does pyrite act as an important host for molybdenum in modern and ancient euxinic sediments? Geochimica et Cosmochimica Acta 126, 112-122.

Colodner, D., Edmond, J., and Boyle, E., (1995) Rhenium in the Black Sea: comparison with molybdenum and uranium. Earth and Planetary Science Letters, 131, 1-15.

Cook, N., Ciobanu, C., George, L., Zhu, Z.-Y., Wade, B., and Ehrig, K. (2016) Trace element analysis of minerals in magmatic-hydrothermal ores by laser ablation inductively-coupled plasma mass spectrometry: Approaches and opportunities, Minerals 6, 111.

Cook, N.J. and Chryssoulis, S.L. (1990) Concentrations of invisible gold in the common sulfides. The Canadian Mineralogist 28, 1-16.

Danyushevsky, L., Robinson, P., Gilbert, S., Norman, M., Large, R., McGoldrick P., and Shelley, M. (2011) Routine quantitative multi-element analysis of sulphide minerals by laser ablation ICP-MS: Standard development and consideration of matrix effects. Geochemistry: Exploration, Environment, Analysis, 11, 51-60.

Deditius, A.P., Utsunomiya, S., Renock, D., Ewing, R.C., Ramana, C.V., Becker, U. and Kesler, S.E. (2008) A proposed new type of arsenian pyrite: Composition, nanostructure and geological significance. Geochimica et Cosmochimica Acta, 72, 2919-2933.

Dornan, T., O'Sullivan, G., O'Riain, N., Stueeken, E., and Goodhue, R. (2020) The application of machine learning methods to aggregate geochemistry predicts quarry source location: An example from Ireland. Computers & Geosciences, 104495.

Emerson, S.R. and Huested, S.S. (1991). Ocean anoxia and the concentrations of molybdenum and vanadium in seawater. Marine Chemistry, 34, 177-196.

Fleet, M.E.A.M., Hamid, A., (1997) Gold-bearing arsenian pyrite and marcasite and arsenopyrite from Carlin Trend gold deposits and laboratory synthesis. American Mineralogist, 82, 182-193.

Gadd, M.G., Layton-Matthews, D., Peter, J.M., and Paradis, S.J. (2016) The world-class Howard's Pass SEDEX Zn-Pb district, Selwyn Basin, Yukon. Part I: trace element compositions of pyrite record input of hydrothermal, diagenetic, and metamorphic fluids to mineralization. Mineralium Deposita 51, 319-342.

Gadd, M.G., Peter, J.M., Jackson, S.E., Yang, Z., and Petts, D. (2019) Platinum, Pd, Mo, Au and Re deportment in hyper-enriched black shale Ni-Zn-Mo-PGE mineralization, Peel River, Yukon, Canada, Ore Geology Reviews, 107, 600-614.

Genna, D. and Gaboury, D. (2015) Deciphering the Hydrothermal Evolution of a VMS System by LA-ICP-MS Using Trace Elements in Pyrite: An Example from the Bracemac-McLeod Deposits, Abitibi, Canada, and Implications for Exploration. Economic Geology, 110, 2087-2108.

Gilbert, S., Danyushevsky, L., Goemann, K., and Death, D. (2014) Fractionation of sulphur relative to iron during laser ablation-ICP-MS analyses of sulphide minerals: implications for quantification. Journal of Analytical Atomic Spectrometry, 29, 1024-1033.

Gilbert, S., Danyushevsky, L., Rodemann, T., Shimizu, N., Gurenko, A., Meffre, S., Thomas, H., Large, R., and Death, D. (2014) Optimisation of laser parameters for the analysis of sulphur isotopes in sulphide minerals by laser ablation ICP-MS. Journal of Analytical Atomic Spectrometry, 29, 1042-1051.

Gregory, D., Meffre, S. and Large, R. (2013) Mineralogy of metal contaminated estuarine sediments, Derwent estuary, Hobart, Australia: implications for metal mobility. Australian Journal of Earth Sciences, 60, 589-603.

Gregory, D., Meffre, S., and Large, R. (2014) Comparison of metal enrichment in pyrite framboids from a metal-enriched and metal-poor estuary. American Mineralogist, 99, 633-644.

Gregory, D.D., Cracknell, M.J., Large, R.R., McGoldrick, P., Kuhn, S., Maslennikov, V.V., Baker, M.J., Fox, N., Belousov, I., and Figueroa, M.C., (2019). Distinguishing Ore Deposit Type and Barren Sedimentary Pyrite Using Laser Ablation-Inductively Coupled Plasma-Mass Spectrometry Trace Element Data and Statistical Analysis of Large Data Sets. Economic Geology, 114, 771-786.

Gregory, D.D., Large, R.R., Bath, A.B., Steadman, J.A., Wu, S., Danyushevsky, L., Bull, S.W., Holden, P., and Ireland, T.R. (2016) Trace Element Content of Pyrite from the Kapai Slate, St. Ives Gold District, Western Australia. Economic Geology, 111, 1297-1320.

Gregory, D.D., Large, R.R., Halpin, J.A., Baturina, E.L., Lyons, T.W., Wu, S., Danyushevsky, L., Sack, P.J., Chappaz, A., and Maslennikov, V.V. (2015) Trace Element Content of Sedimentary Pyrite in Black Shales. Economic Geology, 110, 1389-1410.

Gregory, D.D., Large, R.R., Halpin, J.A., Steadman, J.A., Hickman, A.H., Ireland, T.R., and Holden, P. (2015) The chemical conditions of the late Archean Hamersley basin inferred from whole rock and pyrite geochemistry with Δ 33 S and δ 34 S isotope analyses. Geochimica et Cosmochimica Acta, 149, 223-250.

Gregory, D.D., Lyons, T.W., Large, R.R., Jiang, G., Stepanov, A.S., Diamond, C., Figueroa, M., and Olin, P. (2017) Whole rock and discrete pyrite geochemistry as complementary tracers of ancient ocean chemistry: An example from the Neoproterozoic Doushantuo Formation, China. Geochimica et Cosmochimica Acta, 216, 201-220.

Guillong, M., Hametner, K., Reusser, E., Wilson, S.A., and Günther, D. (2005) Preliminary Characterisation of New Glass Reference Materials (GSA-1G, GSC-1G, GSD-1G and GSE-1G) by Laser Ablation-Inductively Coupled Plasma-Mass Spectrometry Using 193 nm, 213 nm and 266 nm Wavelengths. Geostandards and Geoanalytical Research, 29, 315-331.

Haraldsson, C. and Westerlund, S. (1988) Trace metals in the water columns of the Black Sea and Framvaren Fjord. Marine Chemistry, 23, 417-424.

Harmandas, N., Navarro Fernandez, E., and Koutsoukos, P. (1998) Crystal growth of pyrite in aqueous solutions. Inhibition by organophosphorus compounds. Langmuir, 14, 1250-1255.

Helz, G.R., and Vorlicek, T.P., 2019, Precipitation of molybdenum from euxinic waters and the role of organic matter. Chemical Geology, 509, 178-193.

Huerta-Diaz, M.A. and Morse, J.W. (1990) A quantitative method for determination of trace metal concentrations in sedimentary pyrite. Marine Chemistry, 29, 119-144.

Huerta-Diaz, M.A. and Morse, J.W., (1992) Pyritization of trace metals in anoxic marine sediments. Geochimica et Cosmochimica Acta, 56, 2681-2702.

Jacobs, L., Emerson, S., and Huested, S.S. (1987) Trace metal geochemistry in the Cariaco Trench. Deep-Sea Research. Part A: Oceanographic Research Papers, 34, 965-981.

Kenyon, N.H., Ivanov, M.K., Akhmetzhanov, A.M., and Akhmanov, G.G. (2002) Geological Processes in the Mediterranean and Black Seas and North East Atlantic IOC Technical Series No. 62, UNESCO.

Konhauser, K.O., Planavsky, N.J., Hardisty, D.S., Robbins, L.J., Warchola, T.J., Haugaard, R., Lalonde, S.V., Partin, C.A., Oonk, P.B., and Tsikos, H. (2017) Iron formations: A global record of Neoarchaean to Palaeoproterozoic environmental history. Earth-Science Reviews, 172, 140-177.

Koschinsky, A. and Hein, J.R. (2017) Marine ferromanganese encrustations: Archives of changing oceans. Elements 13, 177-182.

Large, R.R., Halpin, J.A., Danyushevsky, L.V., Maslennikov, V.V., Bull, S.W., Long, J.A., Gregory, D.D., Lounejeva, E., Lyons, T.W., and Sack, P.J. (2014) Trace element content of sedimentary pyrite as a new proxy for deep-time ocean–atmosphere evolution. Earth and Planetary Science Letters, 389, 209-220.

Large, R.R., Maslennikov, V.V., Robert, F., Danyushevsky, L.V., and Chang, Z.S. (2007) Multistage sedimentary and metamorphic origin of pyrite and gold in the giant Sukhoi Log deposit, Lena gold province, Russia. Economic Geology, 102, 1233-1267.

Large, R.R., Mukherjee, I., Gregory, D., Steadman, J., Corkrey, R., and Danyushevsky, L.V. (2019) Atmosphere oxygen cycling through the Proterozoic and Phanerozoic. Mineralium Deposita, 54, 485-506.

Lewis, B.L. and Landing, W.M., (1992)The investigation of dissolved and suspended-particulate trace metal fractionation in the Black Sea. Marine Chemistry, 40, 105-141.

Lyons, T. (1991) Upper Holocene sediments of the Black Sea: summary of leg 4 box cores (1988 Black Sea oceanographic expedition). Black Sea Oceanography, Springer, 401-441.

Lyons, T.W., and Berner, R.A., 1992, Carbon-sulfur-iron systematics of the uppermost deep-water sediments of the Black Sea. Chemical Geology, 99, 1-27.

Lyons, T.W. (1997) Sulfur isotopic trends and pathways of iron sulfide formation in upper Holocene sediments of the anoxic Black Sea. Geochimica et Cosmochimica Acta 61, 3367-3382.

Lyons, T.W., Werne, J.P., Hollander, D.J., and Murray, R.W. (2003) Contrasting sulfur geochemistry and Fe/Al and Mo/Al ratios across the last oxic-to-anoxic transition in the Cariaco Basin, Venezuela. Chemical Geology, 195, 131-157.

Martin, J., P. Nirel and A. Thomas (1987) Sequential extraction techniques: promises and problems. Marine Chemistry, 22, 313-341.

Michel, D., Giuliani, G., Olivo, G.R., and Marini, O.J. (1994) As growth banding and the presence of Au in pyrites from the Santa Rita gold vein deposit hosted in Proterozoic metasediments, Goias State, Brazil. Economic Geology, 89, 193-200.

Morin, G., Noël, V., Menguy, N., Brest, J., Baptiste, B., Tharaud, M., Ona-Nguema, G., Ikogou, M., Viollier, E. and Juillot, F. (2017) Nickel accelerates pyrite nucleation at ambient temperature. Geochemical Perspectives Letters, 5, 6-11.

Morse, J.W. and Arakaki, T. (1993) Adsorption and coprecipitation of divalent metals with mackinawite (FeS). Geochimica et Cosmochimica Acta, 57, 3635-3640.

Mukherjee, I. and Large, R. (2017) Application of pyrite trace element chemistry to exploration for SEDEX style Zn-Pb deposits: McArthur Basin, Northern Territory, Australia. Ore Geology Reviews, 81, 1249-1270.

Mukherjee, I., Large, R.R., Bull, S., Gregory, D.D., Stepanov, A.S., Ávila, J., Ireland, T.R., and Corkrey, R. (2019) Pyrite trace-element and sulfur isotope geochemistry of paleo-mesoproterozoic McArthur Basin: Proxy for oxidative weathering. American Mineralogist: Journal of Earth and Planetary Materials, 104, 1256-1272.

Ostrander, C.M., Sahoo, S.K., Kendall, B., Jiang, G., Planavsky, N.J., Lyons, T.W., Nielsen, S.G., Owens, J.D., Gordon, G.W., and Romaniello, S.J. (2019) Multiple negative molybdenum isotope excursions in the Doushantuo Formation (South China) fingerprint complex redox-related processes in the Ediacaran Nanhua Basin. Geochimica et Cosmochimica Acta, 261, 191-209.

Peiffer, S., Behrends, T., Hellige, K., Larese-Casanova, P., Wan, M., and Pollok, K. (2015) Pyrite formation and mineral transformation pathways upon sulfidation of ferric hydroxides depend on mineral type and sulfide concentration. Chemical Geology, 400, 44-55.

Picard, A., Gartman, A., Clarke, D.R., and Girguis, P.R. (2017) Sulfate-reducing bacteria influence the nucleation and growth of mackinawite and greigite. Geochimica et Cosmochimica Acta, 220, 367-384.

Pisarzowska, A., Berner, Z.A., and Racki, G. (2014) Geochemistry of Early Frasnian (Late Devonian) pyrite-ammonoid level in the Kostomłoty Basin, Poland, and a new proxy parameter for assessing the relative amount of syngenetic and diagenetic pyrite. Sedimentary Geology, 308, 18-31.

Qian, G., Brugger, J., Testemale, D., Skinner, W., and Pring, A. (2013) Formation of As(II)-pyrite during experimental replacement of magnetite under hydrothermal conditions. Geochimica et Cosmochimica Acta, 100, 1-10.

Reich, M. and Becker, U. (2006) First-principles calculations of the thermodynamic mixing properties of arsenic incorporation into pyrite and marcasite. Chemical Geology, 225, 278-290.

Revan, M.K., Genç, Y., Maslennikov, V.V., Maslennikova, S.P., Large, R.R., and Danyushevsky, L.V. (2014) Mineralogy and trace-element geochemistry of sulfide minerals in hydrothermal chimneys from the Upper-Cretaceous VMS deposits of the eastern Pontide orogenic belt (NE Turkey). Ore Geology Reviews, 63, 129-149.

Rickard, D., 2019, Sedimentary pyrite framboid size-frequency distributions: A meta-analysis'. Palaeogeography, Palaeoclimatology, Palaeoecology, 522, 62-75.
Rickard, D. (2012). Sulfidic Sediments and Sedimentary Rocks, Elsevier.
Rickard, D. and Morse, J.W. (2005) Acid volatile sulfide (AVS). Marine Chemistry, 97, 141-197.
Rickard, D.T. (1975) Kinetics and mechanism of pyrite formation at low temperatures. American Journal of Science, 275, 636-652.
Sahoo, S., Planavsky, N., Jiang, G., Kendall, B., Owens, J., Wang, X., Shi, X., Anbar, A., and Lyons, T. (2016) Oceanic oxygenation events in the anoxic Ediacaran ocean. Geobiology, 14, 457-468.
Scott, C., Lyons, T., Bekker, A., Shen, Y., Poulton, S., Chu, X., and Anbar, A. (2008) Tracing the stepwise oxygenation of the Proterozoic ocean. Nature 452, 456-459.
Stepanov, A.S., Danyushevsky, L.V., Large, R.R., Mukherjee, I., and Zhukova, I.A. (2020) Deconvolution of the composition of fine-grained pyrite in sedimentary matrix by regression of time-resolved LA-ICP-MS data. American Mineralogist: Journal of Earth and Planetary Materials, 105, 820-832.
Suits, N. S. and Wilkin, R.T., (1998) Pyrite formation in the water column and sediments of a meromictic lake. Geology, 26, 1099-1102.
Swanner, E.D., Webb, S.M., and Kappler, A. (2019) Fate of cobalt and nickel in mackinawite during diagenetic pyrite formation. American Mineralogist, 104, 917-928.
Tribovillard, N., Algeo, T.J., Lyons, T., and Riboulleau, A. (2006) Trace metals as paleoredox and paleoproductivity proxies: An update. Chemical Geology, 232, 12-32.
Tribovillard, N., Lyons, T.W., Riboulleau, A., and Bout-Roumazeilles, V. (2008) A possible capture of molybdenum during early diagenesis of dysoxic sediments. Bulletin de la Société géologique de France, 179, 3-12.
Vorlicek, T.P., Helz, G.R., Chappaz, A., Vue, P., Vezina, A., and Hunter, W., 2018, Molybdenum burial mechanism in sulfidic sediments: iron-sulfide pathway. ACS Earth and Space Chemistry, 2, 565-76.
Wilkin, R., Barnes, H., and Brantley, S. (1996) The size distribution of framboidal pyrite in modern sediments: An indicator of redox conditions. Geochimica et Cosmochimica Acta, 60, 3897-3912.

Figure Captions

Figure 1: SEM images of framboidal pyrite from the Cariaco basin. A) image of representative framboids cluster from the interval deposited under euxinic conditions (70 cm), both Black Sea and Cariaco Basin pyrite framboids formed under euxinic conditions and look similar to these framboids. B) SEM image of pyrite from the sulfide over print zone of the Cariaco Basin (670 cm). Note the distinct coarsening of the pyrite on the rim edge with an early framboidal pyrite. This is indicative of later, slower pyrite formation after initial nucleation that formed the framboids. This interval also had several euhedral crystals.

Figure 2: LA-ICPMS analyses of pyrite with depth of sediment core from the Cariaco Basin.

Figure 3: LA-ICPMS analyses of pyrite with depth of sediment core from core 315 from the Black Sea.

Figure 4: LA-ICPMS analyses of pyrite with depth of sediment core from core 330 from the Black Sea.

Figure 5: Detailed view of the top 200 cm of the Cariaco Basin analyses for Cu and Ag. These elements show most clearly the increase in TE down core over the first 70 cm.

Tables

Table 1: Median and MAD for LA-ICPMS pyrite TE analyses from different sample depths in the Cariaco Basin.

Depth	Data Source	n	stat	Co	Ni	Cu	Zn	Mo	Ag	Pb	Bi
				ppm	ppm	ppm	ppm	ppm	ppm	ppm	ppm
total		175	median	26.7	294	283	487	649	3.09	54.1	1.40
-2.5	this study	5	median	6.95	175	27.6	611	168	*0.65*	35.7	*0.35*
-27.5	this study	2	median	6.21	93.0	93.9	690	1390	2.50	15.3	*0.31*
-42.5	this study	4	median	3.30	40.9	183	480	949	3.34	22.7	1.75
-70	this study	7	median	16.0	411	363	695	972	7.14	49.6	2.11
-70	Large et al., 2014	28	median	24.8	264	355	689	1030	6.96	43.0	1.83
-115	this study	7	median	20.6	425	287	434	1020	4.16	32.7	1.67
-160	this study	5	median	26.9	473	392	538	747	3.09	66.4	2.27
-295	this study	3	median	15.8	164	496	667	1230	16.2	94.3	1.76
-320	this study	6	median	15.4	372	293	493	1060	5.43	50.4	1.92
-340	Large et al., 2014	4	median	15.6	402	894	650	1490	22.3	115	3.86
-362.5	this study	2	median	5.49	378	1850	609	2310	36.8	111	4.49
-365	Large et al., 2014	14	median	50.5	667	747	536	891	11.2	128	2.84
-450	Large et al., 2014	9	median	110	527	409	722	935	6.51	71.9	2.32
-455	Large et al., 2014	3	median	72.3	300	571	1020	742	7.93	61.9	2.15
-610	this study	1	median	83.5	563	257	205	261	0.71	62.6	1.45
-635	Large et al., 2014	11	median	36.0	311	442	617	698	3.25	67.4	1.86
-640	this study	6	median	25.4	259	544	434	904	4.45	63.1	1.21
-660	this study	9	median	37.9	303	193	355	75.3	1.49	67.4	1.57
-670	this study	10	median	22.0	280	63.5	253	34.9	0.47	35.0	0.73
-670	Large et al., 2014	16	median	33.8	229	34.3	295	34.3	0.38	43.7	0.32
-705	this study	11	median	76.8	272	23.7	82.5	9.19	0.59	40.3	*0.31*
-725	this study	12	median	8.08	21.1	14.1	27.8	4.02	0.24	11.5	*0.23*
Total		175	MAD	18.2	170	216	208	585	2.63	27.9	0.91
-2.5	this study	5	MAD	0.56	126	15.2	170	104	0.05	25.6	0.04
-27.5	this study		MAD	2.53	27.7	11.0	94.6	0.02	0.08	5.78	0.02
-42.5	this study	4	MAD	1.13	11.0	83.4	185	538	2.27	14.2	0.98
-70	this study	7	MAD	5.65	178	73.5	138	197	3.25	3.52	0.64
-70	Large et al., 2014	28	MAD	14.6	171	132	171	322	2.98	19.4	0.85
-115	this study	7	MAD	12.1	288	132	59.9	148	1.88	8.69	0.52
-160	this study	5	MAD	1.47	178	83.0	68.2	306	0.94	5.12	0.14
-295	this study	3	MAD	4.92	20.0	305	23.4	247	13.2	15.2	0.46
-320	this study	6	MAD	9.14	185	192	173	331	2.23	17.7	0.67
-340	Large et al., 2014	4	MAD	7.82	132	98.4	96.9	365	3.31	40.8	1.10
-362.5	this study	2	MAD	0.98	125	427	12.3	906	3.84	22.0	0.81
-365	Large et al., 2014	14	MAD	22.0	174	227	89.8	202	5.77	30.3	1.04
-450	Large et al., 2014	9	MAD	47.0	173	92.1	173	468	1.91	13.0	1.20
-455	Large et al., 2014	3	MAD	1.33	173	75.2	8.98	511	5.65	52.4	1.83

-610	this study	1	MAD	0.00	0.00	0.00	0.00	0.00	0.00	0.00	0.00
-635	Large et al., 2014	11	MAD	11.9	68.4	147	124	212	0.99	34.1	0.89
-640	this study	6	MAD	10.2	94.6	146	51.9	214	0.42	20.6	0.38
-660	this study	9	MAD	19.8	120	118	150	32.8	0.75	28.7	1.06
-670	this study	10	MAD	14.4	113	15.9	58.9	7.32	0.26	21.5	0.21
-670	Large et al., 2014	16	MAD	18.4	85.1	18.5	60.1	8.58	0.23	22.1	0.17
-705	this study	11	MAD	34.7	75.6	19.7	47.1	2.17	0.50	23.8	0.20
-725	this study	12	MAD	3.02	6.28	7.28	12.2	0.91	0.10	4.88	0.07

676 **italics mean that >50% of the samples from that depth had values below detection limits*

677 Table 2: Median and MAD for LA-ICPMS pyrite TE analyses from different sample depths in the Black Sea
678 core 315.

Depth	Unit	n	Stat	Co	Ni	Cu	Zn	Mo	Ag	Pb	Bi
				ppm	ppm	ppm	ppm	ppm	ppm	ppm	ppm
total		39	median	427	986	1090	150	1220	3.04	93.8	3.95
10-12	UI	6	median	37.5	212	566	158	683	2.72	114	4.66
12-14	UI	4	median	51.4	129	467	77.8	428	2.52	135	2.42
14-16	UI	6	median	997	1100	994	145	1900	3.26	83.7	4.89
20-22	UI	5	median	690	745	1610	142	1210	5.43	125	7.45
27-29	UII	9	median	645	1180	1180	154	1550	2.85	63.4	2.64
36-38	UII	6	median	306	1450	1720	351	1480	6.61	92.4	4.20
41-43	UII	3	median	1340	1400	1730	146	1220	2.81	194	3.69
total		39	MAD	345	520	499	46.6	480	1.85	32.6	1.76
10-12	UI	6	MAD	10.6	45.7	157	43.0	76.9	0.81	19.4	0.78
12-14	UI	4	MAD	8.50	40.7	73.5	28.0	207	1.17	9.75	0.27
14-16	UI	6	MAD	520	125	277	37.9	65.3	1.59	22.4	1.33
20-22	UI	5	MAD	326	321	712	41.2	217	2.45	34.8	0.61
27-29	UII	9	MAD	156	203	359	30.3	118	1.53	27.3	0.59
36-38	UII	6	MAD	109	319	133	152	114	2.86	36.4	1.22
41-43	UII	3	MAD	345	199	131	61.2	300	1.18	15.1	0.71

679

680 Table 3: Median and MAD for LA-ICPMS pyrite TE analyses from different sample depths in the Black Sea
681 core 330.

Depth	Unit	n	Stat	Co	Ni	Cu	Zn	Mo	Ag	Pb	Bi
				ppm	ppm	ppm	ppm	ppm	ppm	ppm	ppm
total		35	median	67.0	195	225	177	359	2.14	110	2.82
0-2	UI	5	median	18.4	18.0	58.6	110	54.1	1.85	148	2.33
2-4	UI	6	median	67.2	198	299	177	302	2.18	87.0	2.15
4-6	UI	4	median	42.3	383	754	350	1330	3.59	168	3.56
6-8	UI	6	median	60.2	174	198	160	365	2.54	53.0	2.95
8-10	UI	5	median	964	595	149	434	969	1.59	208	2.56
10-14	UI	9	median	68.4	127	154	177	415	2.32	44.1	2.98
total		35	MAD	45.8	120	118	89.4	189	0.99	72.2	1.59
0-2	UI	5	MAD	13.3	10.6	30.9	22.7	39.6	0.68	44.3	1.25
2-4	UI	6	MAD	19.6	31.2	55.6	61.4	188	0.44	40.7	1.24
4-6	UI	4	MAD	27.9	129	191	74.3	491	1.84	34.0	0.97

6-8	UI	6	MAD	14.7	37.6	30.9	17.3	79.1	1.44	8.10	0.30
8-10	UI	5	MAD	912	458	35.6	84.6	497	1.40	77.8	2.39
10-14	UI	9	MAD	47.5	79.3	138	71.6	161	1.86	37.2	1.74

682

683 Table 4: Median % error

Basin	Co59	Ni60	Cu65	Zn66	Mo95	Ag107	Pb206	Bi209
Cariaco	23	11	15	10	5	20	14	17
Black Sea	4	4	6	20	4	17	16	9

684

685 Table 5: Comparison of pyrite chemistry between the Cariaco Basin and Black Sea

Depth	n	Stat	Co	Ni	Cu	Zn	Mo	Ag	Pb	Bi
			ppm	ppm	ppm	ppm	ppm	ppm	ppm	ppm
Black Sea 315	29	median	645	1180	1370	154	1480	3.75	86.1	3.91
Cariaco 70-640	106		26.7	418	440	603	965	6.19	62.4	2.12
Black Sea / Cariaco Basin pyrite chemistry			24.1	2.82	3.11	0.26	1.54	0.61	1.38	1.84
Black Sea average bulk sediment concentration (Algeo and Lyons, 2003)							45			
Cariaco average bulk sediment concentration (Algeo and Lyons, 2003)							85			
Black Sea / Cariaco Basin bulk chemistry							0.53			

686

687

Figure 1

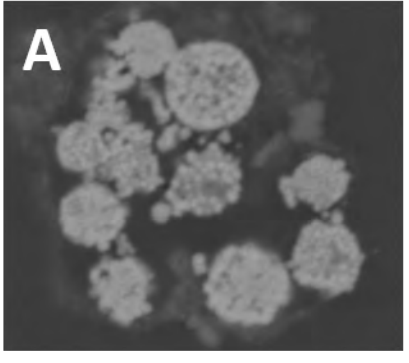

10 µm

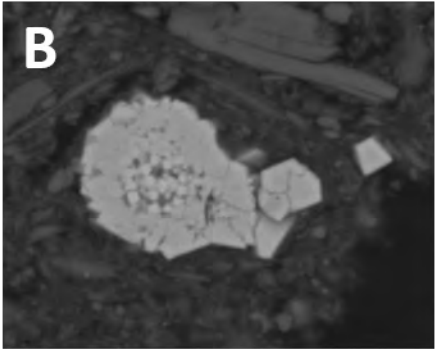

10 µm

Figure 2

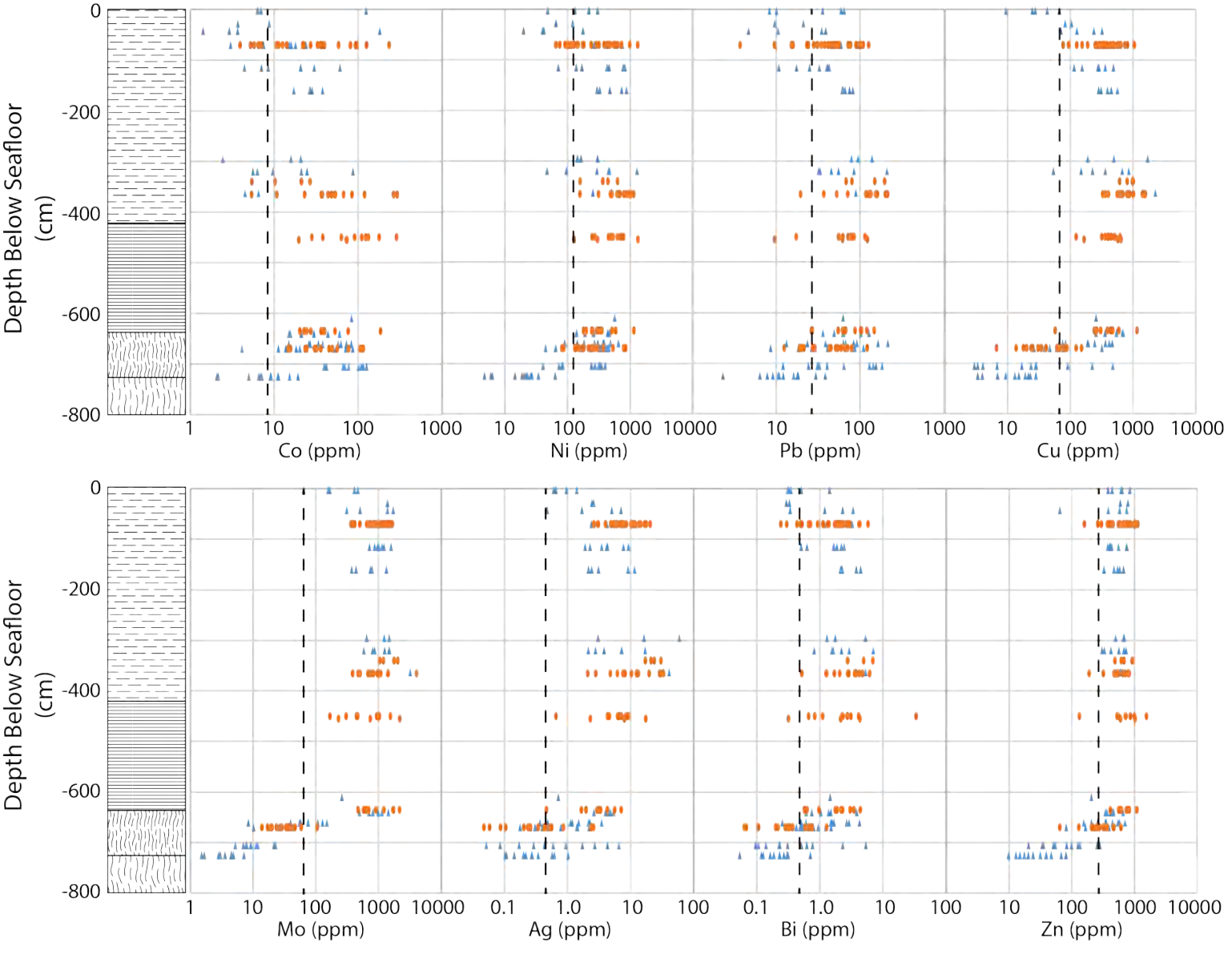

Microlaminated, dark olive gray, organic-rich silty clay with nannofossils and foraminifera deposited under euxinic conditions

Microlaminated, dark olive gray, organic rich, diatom-rich clayey mud with abundant calcareous microfossils deposited under euxinic conditions.

Massive bioturbated light gray clay. Sulfide diffusion zone of sediments deposited under oxic conditions.

Massive bioturbated reddish-brown clay deposited under oxic conditions.

LA-ICPMS pyrite analysis (Large et al., 2014)

LA-ICPMS pyrite analysis (this study)

Median - MAD

Figure 3

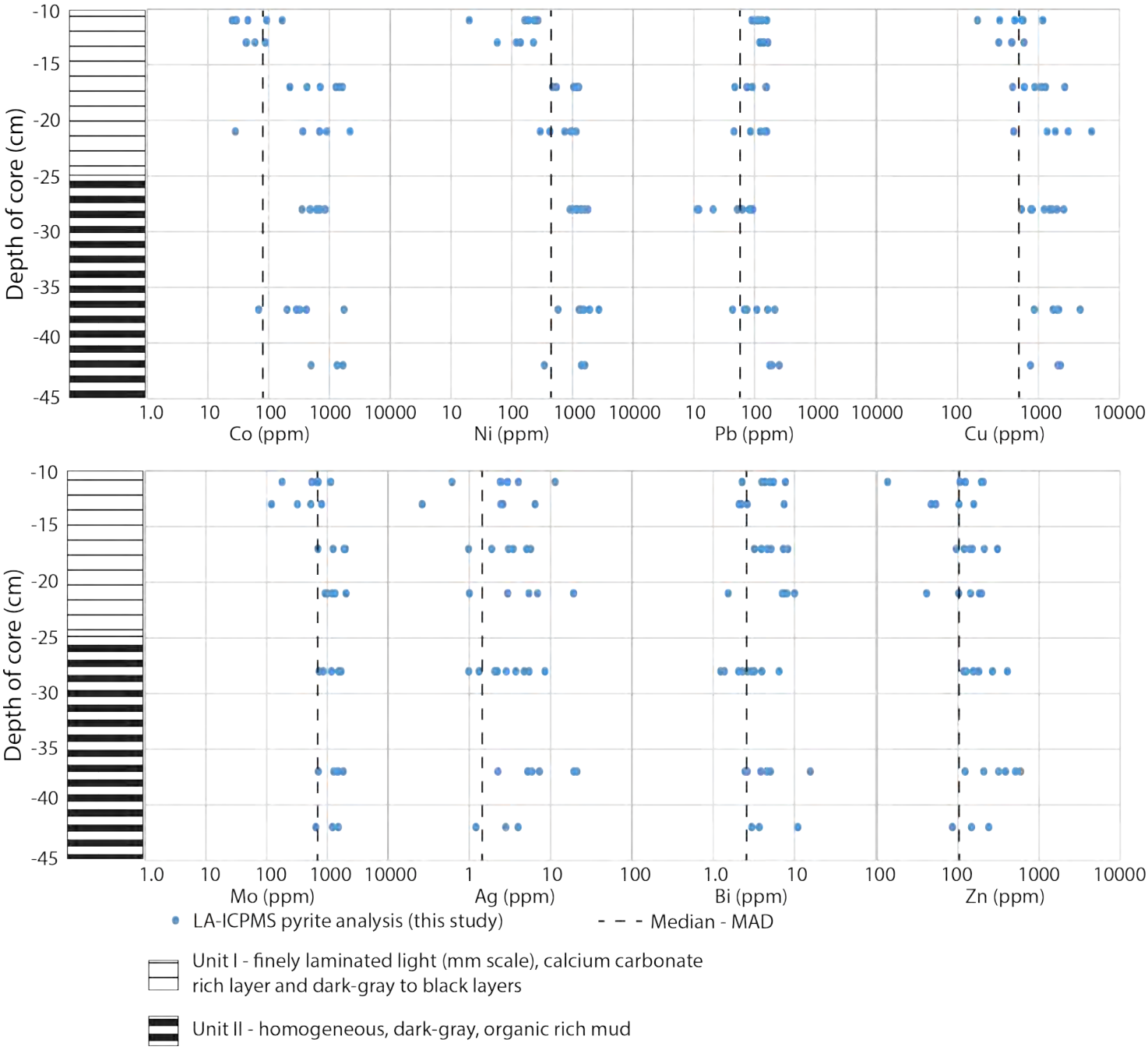
Depth of core (cm)
-10
-15
-20
-25
-30
-35
-40
-45
1.0
10
100
1000
10000
Co (ppm)
Ni (ppm)
Pb (ppm)
Cu (ppm)
Mo (ppm)
Ag (ppm)
Bi (ppm)
Zn (ppm)
LA-ICPMS pyrite analysis (this study)
Median - MAD
Unit I - finely laminated light (mm scale), calcium carbonate rich layer and dark-gray to black layers
Unit II - homogeneous, dark-gray, organic rich mud

Figure 4

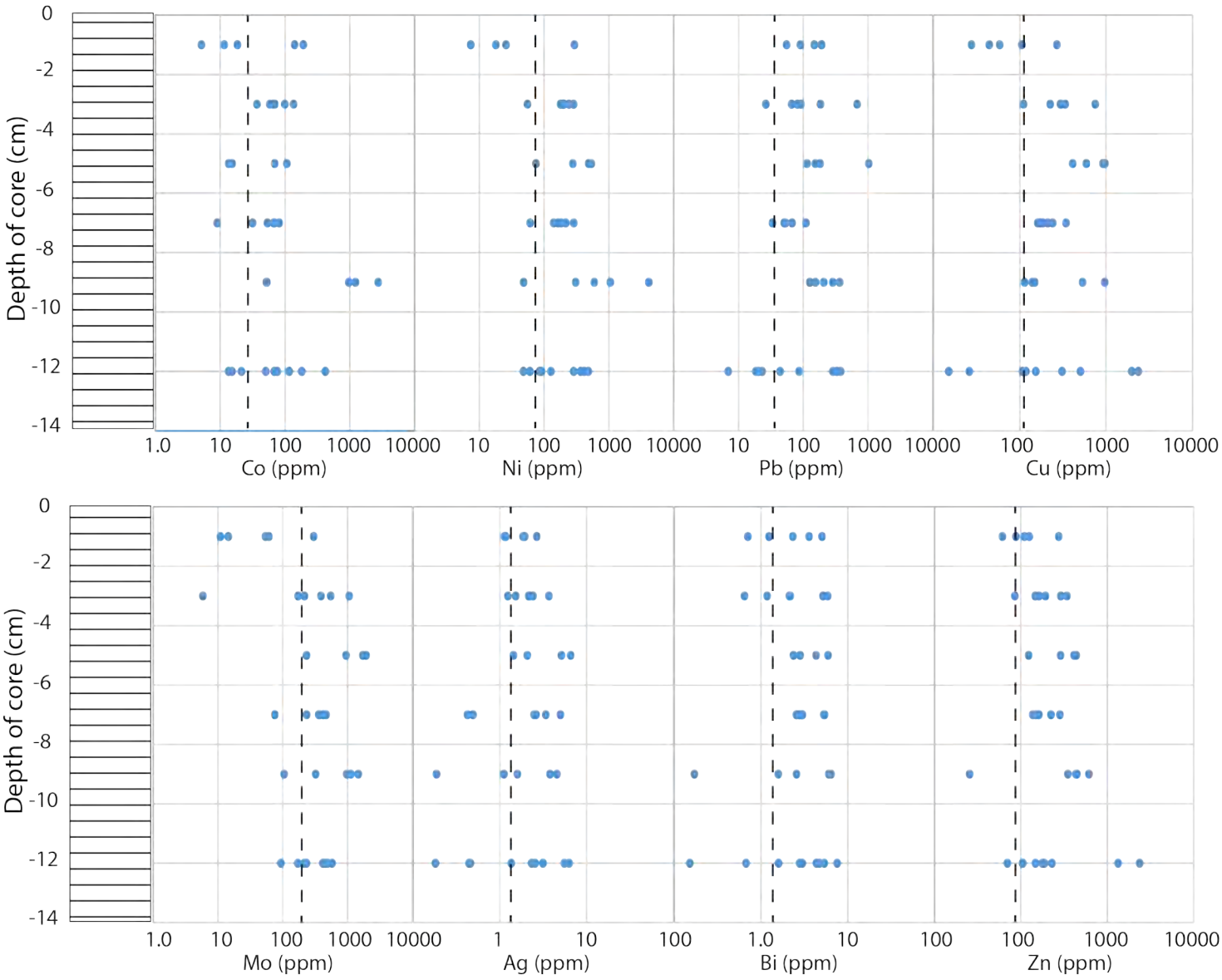
Depth of core (cm)
0
-2
-4
-6
-8
-10
-12
-14
1.0
10
100
1000
10000
Co (ppm)
Ni (ppm)
Pb (ppm)
Cu (ppm)
Mo (ppm)
1
Ag (ppm)
Bi (ppm)
Zn (ppm)
LA-ICPMS pyrite analysis (this study)
Median - MAD
Unit I - finely laminated light (mm scale), calcium carbonate rich layer and dark-gray to black layers

Figure 5

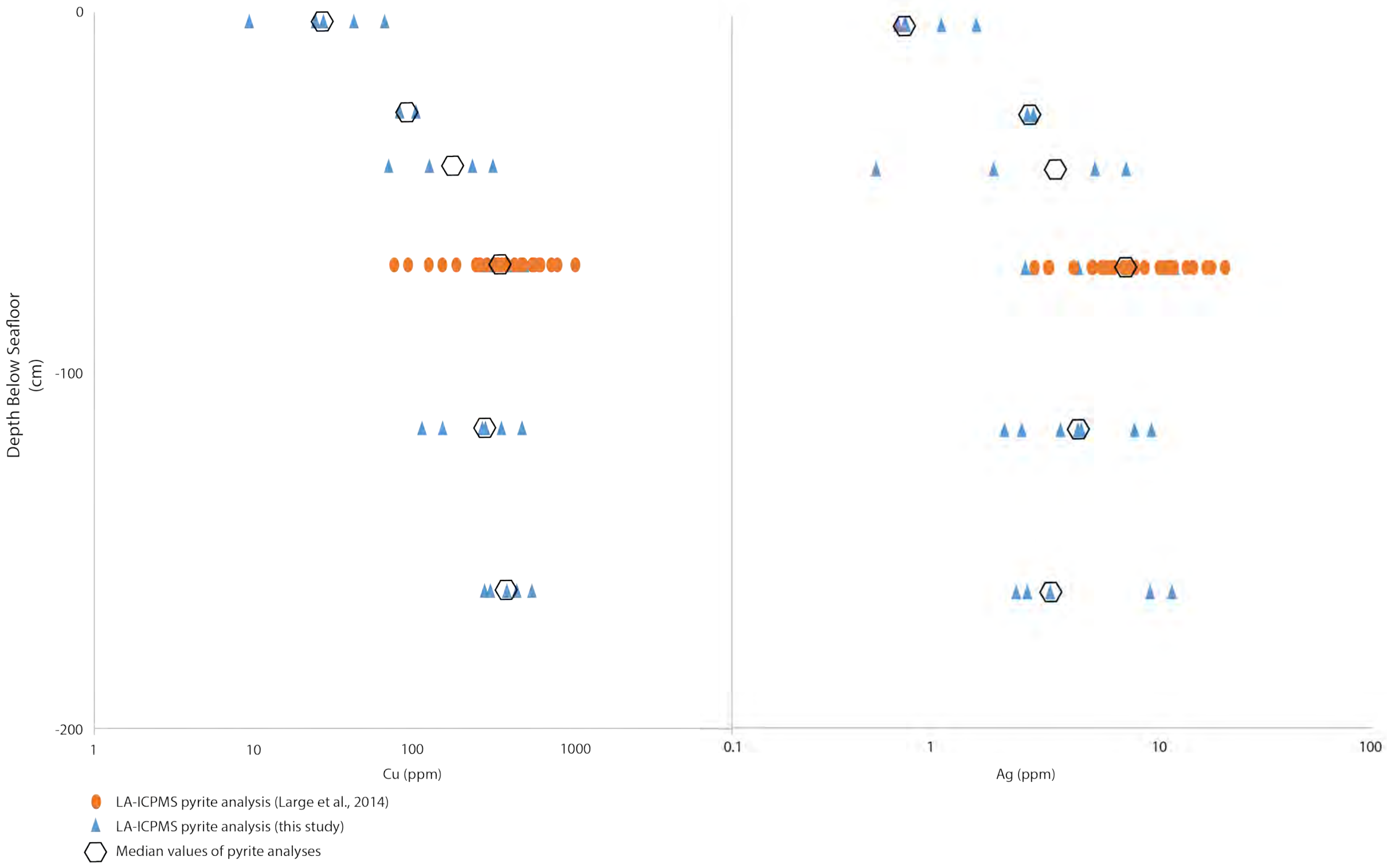
0
-100
-200
Depth Below Seafloor (cm)
1
10
100
1000
Cu (ppm)
0.1
1
10
100
Ag (ppm)
LA-ICPMS pyrite analysis (Large et al., 2014)
LA-ICPMS pyrite analysis (this study)
Median values of pyrite analyses